



Response of runoff to climate change in the Manas River Basin flow-producing area, Northwest China

Xinchen Gu^{1,2} · Aihua Long^{2,3,4} · Xinlin He³ · Hao Wang^{1,2} · Xiaoying Lai⁴ · Ning Pang³ · Huan Liu⁵ · Haoran Yu⁶

Received: 12 September 2022 / Accepted: 27 December 2023 / Published online: 8 February 2024
© The Author(s) 2024

Abstract

The inland river basins of northwestern China are structured as mountain-basin systems. Water resources originate in the flow-producing area (FPA), are utilized and operated in the oasis area and are dissipated in the desert area. In this study, a Soil and Water Assessment Tool (SWAT) model was constructed in the Manas River Basin (MRB) FPA. Meanwhile, it simulated climate change and runoff evolution trends in the FPA of the MRB under different four climate change scenarios of Coupled Model Intercomparison Project Phase 5. The main findings showed that (1) the years 1979–1980 were chosen as the model warm-up period, 1979–2000 as the model calibration period and 2001–2015 as the model validation period to complete the construction of the SWAT model for MRBFPA. From 1981 to 2015, three performance parameters indicated that the model accuracy meets the requirements ($NSE = 0.81$, $R^2 = 0.81$ and $PBIAS = 1.44$) and can be used for further studies; (2) the hydrological elements (e.g. runoff, potential evapotranspiration, evapotranspiration, soil water content, snowmelt) in the MRBFPA were analysed by the constructed SWAT model; (3) the climate change in the MRBFPA is close to the RCP 8.5 scenario, and the future changes in water resources under this scenario will range from 659 to 2308 (million) m^3 . Compared to the multi-year historical mean value ($12.95 \times 10^8 m^3$), the future fluctuation in the amount of water resources available in this basin is increasing.

Keywords SWAT model · CMIP5 · Manas River Basin flow-producing areas · Northwest China · Tianshan mountains

Introduction

Water resources are particularly important to human society and the natural environment. As a result of socioeconomic development and the construction of water resources projects, the total amount and manner of water extraction and use by human beings have changed (Hu, 2021). Since the industrial revolution, global warming has accelerated or slowed down regional water cycle processes. The manifestations are different in different regions: frequent heavy rainfall and flooding (Tian, 2023), accelerated melting of glaciers and snow (Sorg, 2012), frequent heat waves and droughts (Gu, 2023; Williams, 2022) and degradation of ecosystems (Guglielmi 2022). At the same time, changes in the subsurface affect the flow-producing process, and the construction of reservoirs, dams and canals changes the catchment process. Therefore, a deep understanding of the local hydrological cycle is necessary to provide theoretical support for improved water resource management.

Climate change has an impact on water resources formation through its influence on mountain ice melt, snowmelt

✉ Aihua Long
ahlong@iwhr.com

✉ Xinlin He
hexinlin2002@163.com

¹ State Key Laboratory of Hydraulic Engineering Simulation and Safety, School of Architectural Engineering, Tianjin University, Tianjin 300072, China

² State Key Laboratory of Basin Water Cycle Simulation and Regulation, China Institute of Water Resources and Hydropower Research, Beijing 100044, China

³ Key Laboratory of Modern Water-Saving Irrigation of XPCC, College of Water Conservancy and Architectural Engineering, Shihezi University, Shihezi 330022, China

⁴ College of Management and Economics, Tianjin University, Tianjin 300072, China

⁵ Zhuhai ORBITA Aerospace Science and Technology Co., Ltd., Zhuhai 519000, China

⁶ School of Landscape Architecture, Nanjing Forestry University, Nanjing 210037, China

and precipitation. On the other hand, socioeconomic development also has a huge impact on water demand. According to the Fifth Assessment Report of the Intergovernmental Panel on Climate Change (IPCC AR5), the average global temperature rose by 0.85 °C between 1880 and 2012 (Intergovernmental Panel on Climate Change, 2018). From 1951 to 2020, the average annual surface temperature in China showed a significant upward trend, with a warming rate of 0.26 °C/decade, significantly higher than the global average (0.15 °C/decade) during the same period; the average annual precipitation in China showed an increasing trend, with an average increase of 5.5 mm (Center on Climate Change, CMA, 2020). In contrast, the NWC is highly sensitive to global climate change. Since 1961, when meteorological observations became available, the rate of increase in temperature in the NWC has been 0.333 °C/decade; the average precipitation increase trend has been 8.8 mm/decade (Yi Liu 2019). A cautionary note is that the increase in temperature in the NWC far exceeds the global average, and the resulting potential evapotranspiration continues to increase, far exceeding the increase in precipitation in some regions, leading to more severe aridification in these regions, and more dehydrated (Thomas 2000; Geng et al. 2016; Li et al. 2018b).

Water resources are a strong constraint on socioeconomic development in the arid regions of northwest China (NWC) (Kang et al. 2017), especially with the rapid expansion of oasis agriculture in recent decades, with agricultural irrigation accounting for more than 85% of total water consumption in the basin (Mingjiang 2018; Water Resources Department of the Ministry of Water Resources 2021). Irrational irrigation patterns, inadequate water facilities and rapid expansion of crop areas have exacerbated water scarcity, with agricultural water seriously crowding out ecological water, causing widespread ecological degradation and river cut-off problems (Li et al. 2018a; Cheng and Li 2018).

The MRB is a typical basin in the NWC. For more than 50 years, the MRB has seen the construction and renovation of a large number of hydraulic projects about agricultural irrigation: conversion of natural rivers into channels and extensive construction of reservoirs. Grasslands/wetlands were converted into arable land through the promotion of irrigation (He et al. 2018). In recent years, however, studies have shown that the ecology of the MRB is in a precarious state, and the ecological environment continues to deteriorate (Yang et al. 2019, 2020). This is because humans have seized ecological water resources for socioeconomic development (Ling et al. 2012; Yang et al. 2017). With this irrational allocation, the impact of climate change on the amount of water resources may cause an ecological disaster. The MRB flow-producing area, as the main source of supply of water resources in the basin (Liu et al. 2019; Gu et al. 2020), must be clarified in terms of the response of its runoff

to climate change. This is a prerequisite for the rational use of water resources in the basin.

The previous studies about hydrological process in the MRB mainly focused on the interrelationship between runoff and climate change. The study of the mechanisms that reveal the response of runoff to climate change in the flow-producing areas of the MRB, however, is not yet completed. When we want to simulate and analyse the changes in runoff and water resources in the MRBFPA, more detailed climate change scenarios should be considered. Therefore, in this study, the aims are as follows: (1) the SWAT model for the MRBFPA is constructed; (2) the hydrological components of the MRBFPA are analysed; and (3) the four main climate change scenarios (RCP 2.6, 4.5, 6.0 and 8.5) in CMIP 5 are used to analyse the runoff response and future changes in available water resources.

Method and data

Overview of the study area

The MRB lies at the heart of the Eurasian continent. It is also the core of the economic development zone on the northern slopes of the Tian Shan Mountains. The MRB extends from the Ilian Habir Ga Mountains in the south to the southern edge of the Gurbantunggut Desert in the north, and is bordered on the east and west by the Tasi River Basin and the Bayingou River Basin, respectively. Its geographical range is from 43°07'N to 45°51'N and 85°01'N to 86°35'E (Fig. 1). The Manas River flows into the Junggar Basin from the basin's FPA, gathering tributaries such as the Lama Temple Ditch, Haxiong Ditch, Dabaiyang Ditch, Xiaobaiyang Ditch and the Qingshui River along the way. With a total length of 324 km, the Manas River is the longest river on the southern edge of the Gurbantunggut Desert, with an average annual runoff of $12.95 \times 10^8 \text{ m}^3$ and a basin area of $34,050 \text{ km}^2$. The administrative scope of the MRB includes Shihezi City, the Eighth Division of the Xinjiang Production and Construction Corps (XPCC), Manas County and its 10 townships, the Xinhu General Farm of the Sixth Division of the XPCC, five townships in Shawan County and Xiaoguai Township in Karamay City.

The MRBFPA is located in the southern part of the MRB, which has a geographical range of 43°07'N to 43°58'N and 84°56'E to 86°25'E. The Kenswat Water Conservancy Hub Project, which was officially put into operation in August 2015, was listed as a key project of the Western Development in 2010, and it is also the only one of the largest independently built projects of the XPCC. As the most critical water control hub in the MRB, the project is located in the heart of the Tianshan Northern Foothills urban agglomeration, with the city of Shihezi just 70 km away. The dam is

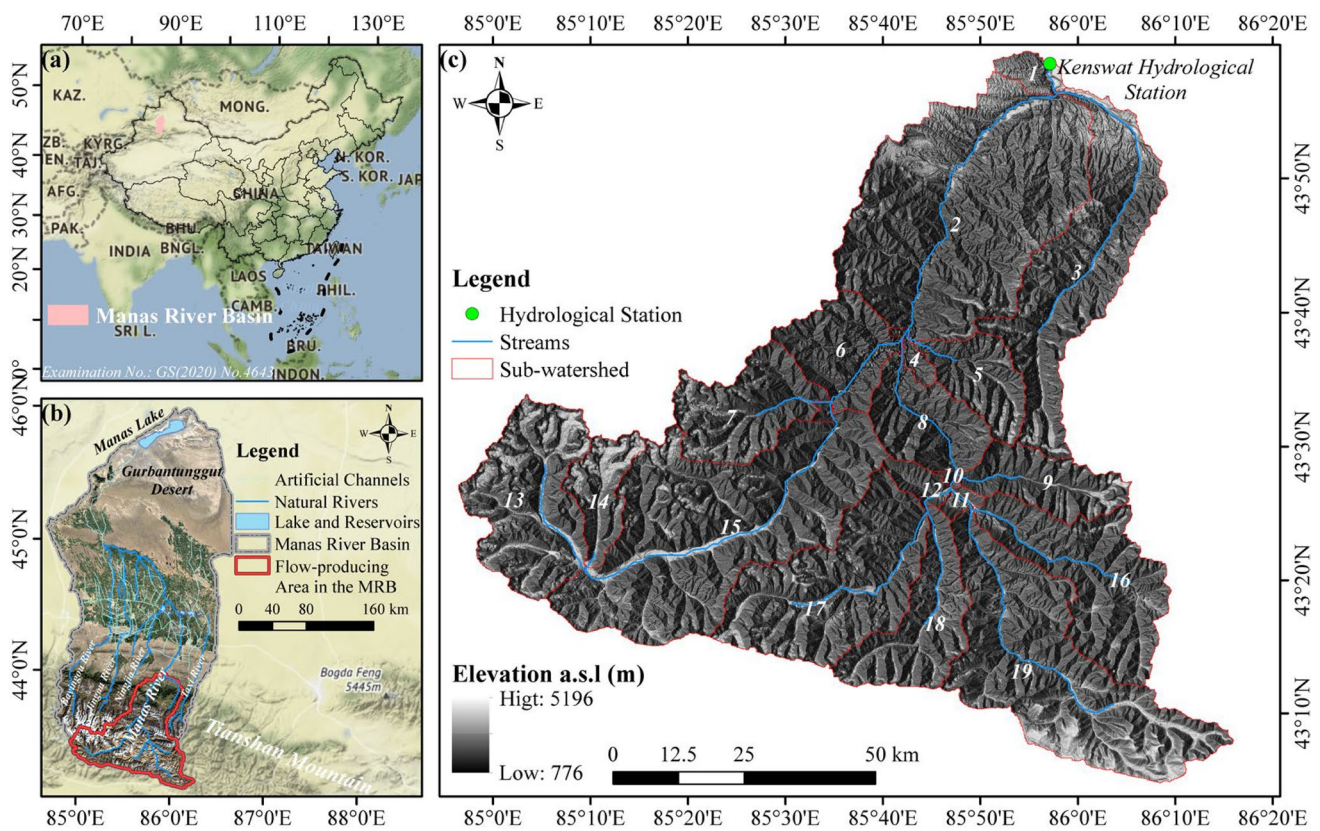


Fig. 1 Overview of the study area **a** location of the Manas River Basin (MRB) in China; **b** distribution of flow-producing area (FPA) and water systems in the MRB; **c** elevation-based delineation of sub-watershed and streams in the MRBFPA

built in a class 8 seismic zone, with a height of 129.4 m, the highest of its kind, and a total reservoir capacity of $1.88 \times 10^8 \text{ m}^3$. The Kenswat hydrological station (85.95°E, 43.98N°) is located at an altitude of 955 m.

Research framework

This study focuses on the future availability of water resources in the MRBFPA. Firstly, we obtained meteorological data, hydrological data, LUCC data, DEM data and soil data of the study area. Secondly, we used software and methods such as ArcSWAT and SWAT-CUP to construct a hydrological model of the MRBFPA. Finally, the changes of hydrological elements in the study area and the changes of total available water resources in the future were obtained. The framework of our study is shown in Fig. 2.

Data sources and processing

LUCC data

The LUCC data used in this study were obtained through Landsat series satellite image interpretation, and the remote sensing image data were downloaded through the Geospatial

Data Cloud (<http://www.gscloud.cn/>). Landsat-8 remote sensing image data were used to obtain the 2015 land use in the MRBFPA. Landset images were selected for the same period (June–August), with abundant feature images and low cloudiness. The classification criteria for land use interpretation were classified using the Chinese Academy of Sciences secondary land use classification criteria. Land use data at 30 m spatial resolution in the MRBFPA were obtained using the ArcGIS resampling tool according to the needs of the study.

Soil data

Soil data for the study area, the MRBFPA, were obtained from the Harmonised World Soil Database (HWSD) V1.2 dataset created by the FAO and the International Institute for Applied Systems (IIASA), Vienna. The soil data for this study area, the MRBFPA, were obtained using the ArcGIS cropping tool. The relevant soil physical and chemical properties are available on the HWSD website (<http://www.fao.org/>, access on 20 July 2022). The physical parameters of the soil type data required for the SWAT model of the MRBFPA were calculated using SPAW software based on the soil

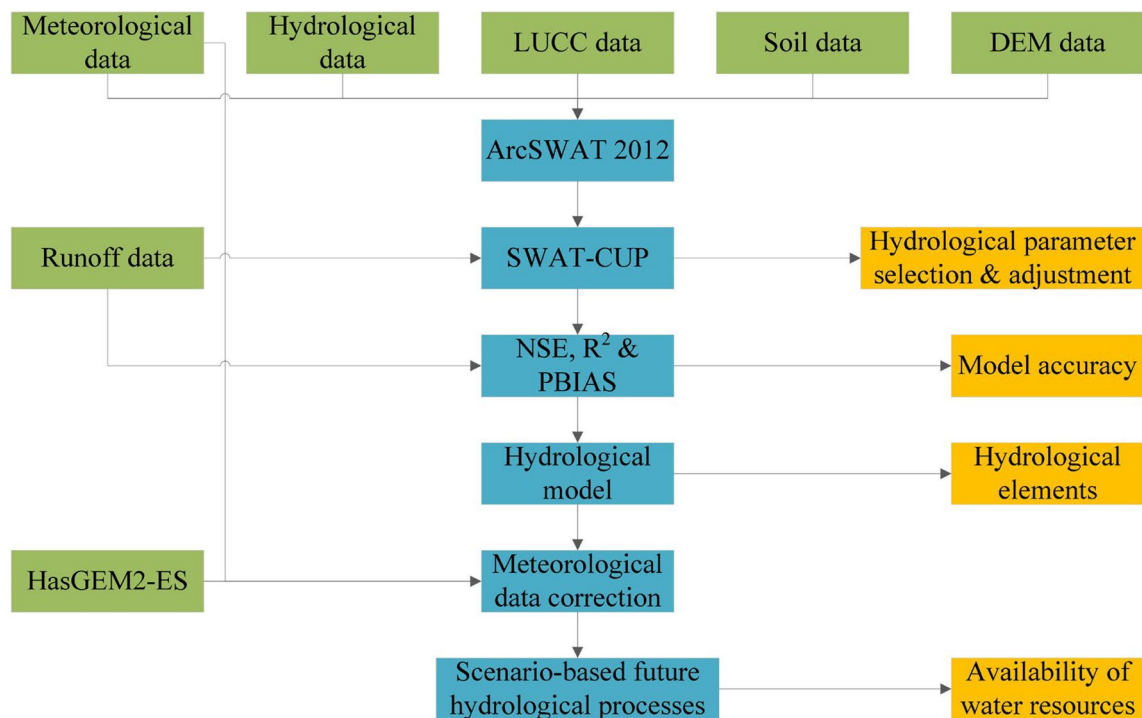


Fig. 2 Research framework, describing the relationship between data, methods, models, and results

physicochemical properties provided by HWSO (Appendix: Table 6).

DEM data

This study uses DEM data sources with data from the Japanese Earth Observation Advanced Land Observing Satellite (ALOS), downloaded through the National Aeronautics and Space Administration (NASA) website (<https://search.earthdata.nasa.gov/>, access on 20 July 2022). The mission objectives of ALOS (Igarashi 2001) are cartography, regional observations, disaster monitoring and land resource exploration for science and applications. ALOS will provide global high spatial resolution Earth observation datasets from three remote sensing instruments. ArcGIS was used to mosaic and crop the downloaded DEM data to obtain 12.5 m resolution DEM data of the MRBFPA. The highest elevation of the MRBFPA is 5146 m and the lowest elevation is 804 m.

Hydrological data

The hydrological data used in this study were the daily runoff flow data from the Kenswat hydrological station, which were obtained from the Kenswat hydrological observation station of the Xinjiang MRB Management Office for the period from 1 January 1981 to 31 December 2016. According to the needs of the study, the daily runoff flow was

calculated to obtain the monthly and annual runoff flow of Kenswat hydrological station, respectively.

Meteorological data

The main meteorological station data used in this study were obtained from the China National Meteorological Administration (<http://data.cma.cn/>, access on 20 July 2022). This study used 13 meteorological stations on the northern slope of Tianshan Mountains (Zhang, 2023), with daily elements such as precipitation, maximum temperature, minimum temperature, evapotranspiration, wind speed, coordinates of each station and elevation, for the period from 1 January 1981 to 31 December 2016.

SWAT model

Model principles

The discretization of the SWAT catchment area is carried out from a given digital elevation model (DEM) to multiple sub-catchments, each of which has a hydrological response unit (HRU) with similar land use and soil types and is the basic model unit (Arnold et al. 2010, 2012). The model simulates the hydrological processes of evapotranspiration, filtration, surface runoff, groundwater runoff and sediment erosion in each HRU (Cho et al. 2012; Ghaffari et al. 2010; Pereira et al. 2016), with runoff from each HRU first converging into

the mainstem of each sub-catchment and then flowing from one sub-catchment to another before reaching the outlet of the catchment. The water balance equation for HRU can be expressed as follows (Agr 1980; Luo et al. 2013):

$$SW_t = SW_0 + \sum_{i=1}^t (R_{\text{day}} - Q_{\text{surf}} - E_a - w_{\text{seep}} - Q_{\text{gw}}) \quad (1)$$

where SW_t is the final soil water content, mm; SW_0 is the initial soil water content, mm; t is the simulation time, days; R_{day} is the daily precipitation, mm H_2O ; Q_{surf} is the daily surface runoff, mm H_2O ; E_a is the daily evapotranspiration, mm; w_{seep} is the amount of water entering the air pocket from the soil profile on a given day, mm; Q_{gw} is the return flow on a given date, mm.

Glaciers are widespread in the alpine region of the MRB, and glacier meltwater makes a high contribution to river runoff. Although glacier melt is mainly dependent on its surface energy balance, the application of energy balance models is limited by the need to incorporate many parameters (Qi et al. 2017) and the complexity of calculations for remote, high-altitude mountainous areas (Zaremehrijardy et al. 2021). In this study, a degree-day model based on a linear relationship between snow and ice melt and air temperature was chosen to analyse the effect of glacial meltwater on river runoff. The general form of the degree-day model is:

$$M = \text{DDF} \cdot \text{PDD} + \alpha R \quad (2)$$

where M is the ablated water equivalent of the glacier, mm/d; DDF is the degree-day factor of the glacier, mm/(d · °C); PDD is the positive cumulative temperature, generally obtained from Eq. (3); α is the coefficient, (mm · m²)/MJ; R is the solar shortwave radiation or net radiation, MJ/(mm · d).

$$\text{PDD} = \sum_{t=1}^n H_t \cdot T_t \quad (3)$$

where T_t is the average daily temperature (°C); H_t is a logical variable, when $T_t \geq 0$ °C, $H_t = 1$; when $T_t \leq 0$ °C, $H_t = 0$.

Internal soil flow characteristics in SWAT areas were calculated using dynamic storage models of topographic gradients, soil hydraulic conductivity (**SOL_K**) and spatial and temporal variations in soil moisture. Lateral flow is important in soil catchments with high hydraulic conductivity at the surface. Sloan and Moore (1984) combined SWAT with a subsurface water flow kinematic storage model to simultaneously calculate seepage. The shallow aquifer then collects groundwater into the main channel of the sub-basin. Surface runoff is precipitation after interception of infiltration and surface runoff is estimated using the Green–Ampt infiltration method and the runoff curve number method (SCS) (Boughton, 1989). Flood runoff rates

reflect the erosive power of heavy rainfall and can be used to predict sediment loss. Evapotranspiration includes transpiration from plant canopies and evaporation of soil water and trapped precipitation or dew. Several methods exist for modelling potential evapotranspiration (PET), including the Priestley–Taylor method (PRIESTLEY and TAYLOR 1972), the Penman–Montes method (Monteith 1965) and the Hargreaves method (Hargreaves and Samani 1985), which were incorporated into the SWAT model.

Hargreaves and Samani used the Hargreaves formula based on temperature and solar radiation ET_0 . Because of its better calculation results, the Food and Agriculture Organization of the United Nations (FAO) recommends its use when meteorological information is lacking (Abbaspour et al. 2007; Hargreaves and Allen 2003). The Hargreaves method was used to simulate PET in this study and the equation can be expressed as follows:

$$PET_{\text{har}} = 0.0023R_a \left(\frac{T_x + T_n}{2} + 17.8 \right) \sqrt{T_x - T_n} \quad (4)$$

where T_x is the daily maximum temperature, °C; T_n is the minimum temperature, °C; R_a top-of-atmosphere solar radiation, MJ/(m² · d), which can be calculated from latitude or found from the top-of-atmosphere radiation table provided by FAO.

Model build setup

ArcGIS was opened to load the processed DEM data and the 'burn-in' command was used to load the digital water system. Then, based on the results of previous studies and taking into account the size of the study area and the simulation accuracy of the model (Luo et al. 2012, 2013; Gu et al. 2020; Zhang 2018), the watershed threshold was set to 5000 to generate a watershed network. Secondly, the hydrological station of Kenswat was selected and defined as the total outlet of the watershed to perform watershed delineation. Finally, the calculation of sub-basin parameters and the addition of reservoirs were performed. As the SWAT model only takes into account the role of reservoirs for flow regulation, it is not concerned with their location. The location of the reservoirs in the model is automatically adsorbed to the nearby basin nodes.

The MRBFPA was divided into 19 sub-basins. The Kenswat hydrological station was added as the basin outlet, and this station was selected for basin delineation and calculation. LUCC data were used to reclassify the watershed land use and imported into the model using the 2015 vector land use data for the MRBFPA. Soil data were calculated using HWSO 1.2 soil data for watershed soil data and imported into the SWAT model, and the reclassified soil database is shown in Appendix Table 6. Four categories of

slope classification $0-15^\circ$, $15-25^\circ$, $25-75^\circ$ and $\geq 75^\circ$ were defined. Land use, soil and slope were overlaid for analysis and 747 HRUs were generated (Fig. 3). After delineating the HRUs, the watershed meteorological data were collated and imported into the model. And then the watershed database was written and updated. Finally, a warm-up period of two years was set, the model was selected for the monthly scale, and the 64-bit release version was selected for simulation and written to the database (Fig. 3). The SWAT model of the MRBFPA was constructed. Due to the lack of human activity in the MRBFPA, we used runoff data measured by the Kenswat hydrological station for model calibration and validation.

Model calibration and validation

This study applies the SUFI-2 algorithm in SWAT-CUP 2019 to complete the final estimation by iteratively estimating the unknown parameters through a sequential fitting procedure. The procedure also takes into account the uncertainties in the model inputs, model structure, input parameters and observed data. During the calibration process, the

programme uses a global sensitivity analysis method, which takes into account the equilibrium phenomenon in the rate calibration process and uses the t test (t -Stat) and P test (P Value) methods for sensitivity assessment. Finally, these different parameter settings generate acceptable runoff curves. In this process, the higher the sensitivity of the parameters, the larger the absolute value of t -Stat and the P Value is close to the zero value.

Based on a comprehensive evaluation approach, Moriasi proposed four quantitative statistical methods (Moriasi et al. 2007): the Nash–Sutcliffe coefficient (NSE), percentage bias (PBIAS), relative root mean square error (RRMSE) and relative error (R^2). In this paper, three commonly used methods (NSE, PBIAS and R^2) have been selected to quantify the performance of the model. The purpose of these three performance metrics is to quantify how well the simulated values of the numerical model match the measured values. The NSE is a statistical method that quantifies the relative magnitude of the residual variance (Nash and Sutcliffe 1970), PBIAS indicates that the average trend of the simulated data is greater or less than the average trend of the corresponding observed data (Gupta et al. 1999), which is different from

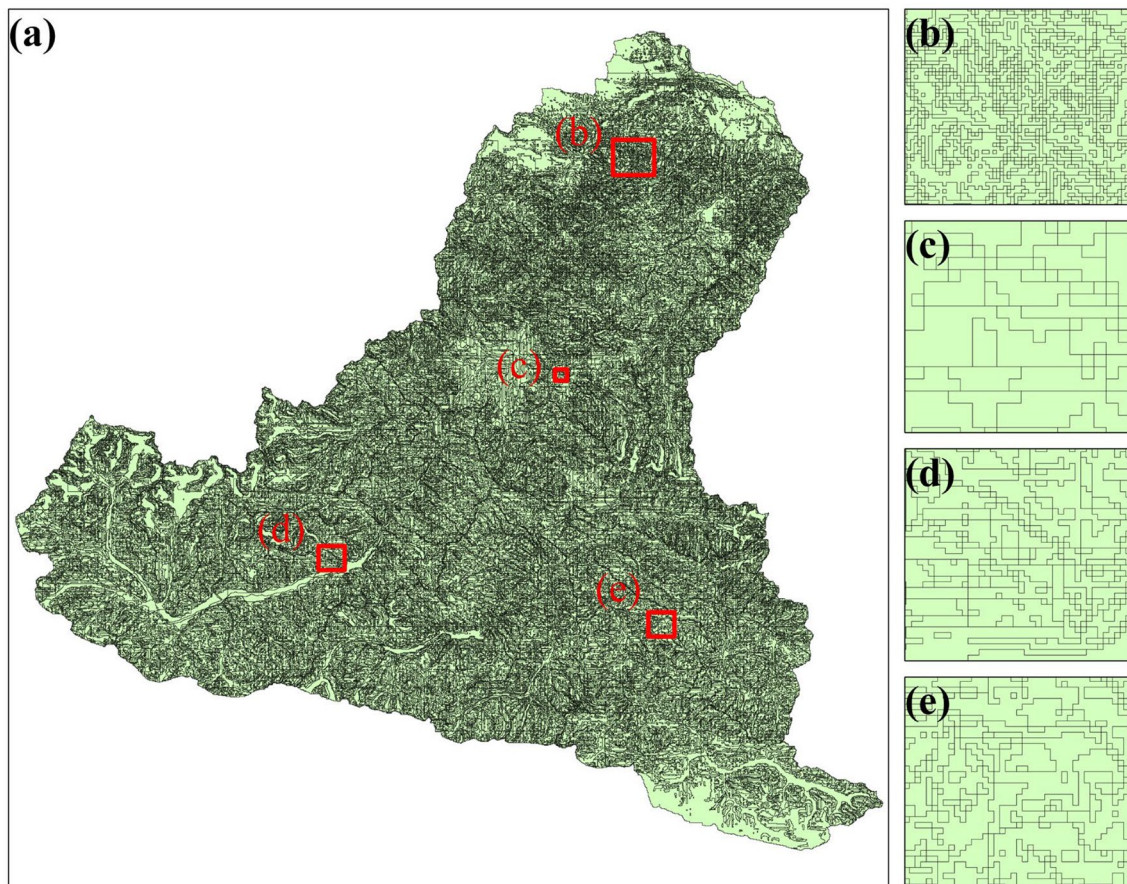


Fig. 3 MRBFPA HRU divisions, **a** the HRU division results of MRBFPA, **b–e**, respectively, show the details of HRU

the variance used for the observed data. The NSE, R^2 and PBIAS equations can be expressed separately as follows:

$$NSE = \frac{\sum_{i=1}^n (o_i - \bar{o})^2 - \sum_{i=1}^n (s_i - o_i)^2}{\sum_{i=1}^n (o_i - \bar{o})^2} \tag{5}$$

$$R^2 = \left[\frac{\sum_{i=1}^n (o_i - \bar{o})(s_i - \bar{s})}{\sqrt{\sum_{i=1}^n (o_i - \bar{o})^2} \sqrt{\sum_{i=1}^n (s_i - \bar{s})^2}} \right]^2 \tag{6}$$

$$PBIAS = 100 \times \left[\frac{\sum_{i=1}^n (o_i - s_i)}{\sum o_i} \right] \tag{7}$$

where R^2 is the square of the correlation coefficient R ; NSE is the Nash–Sutcliffe efficiency factor; PBIAS is the deviation of the evaluated data (expressed as a percentage); o_i is the measured runoff, m^3/s ; s_i is the simulated runoff, m^3/s ; \bar{o} is the average measured runoff during the simulation, m^3/s ; \bar{s} is the average simulated runoff during the simulation, m^3/s ; n is the number of flow measurements in the analysis; and k is the number of independent variables.

Of the three metrics mentioned above, the closer the NSE and R^2 values are to 1, the better the performance of SWAT, while when PBIAS is close to zero, it represents a very accurate simulation. Moriasi (2007) suggests that the model can be used as a satisfactory simulation when $NSE \geq 0.5$ and PBIAS is within $\pm 25\%$, and the criteria developed by Moriasi are used in this paper Table(1).

HasGEM2-ES

The Inter-Sectoral Impact Model Intercomparison Project (ISIMIP) provides historical and future scenario data for the daily-scale HasGEM2-ES model (Frieler et al. 2017; Jones et al. 2011). The time range of the historical data is 1950–2005, and the time range for the four future scenarios (RCP 2.6, 4.5, 6.0 and 8.5) is 2006–2099. The three climate elements provided are precipitation, maximum temperature and minimum temperature, with a spatial resolution of $0.5^\circ \times 0.5^\circ$. The HasGEM2-ES model data were selected for the MRBFPA. The model data were downscaled according

to the location of the meteorological stations used in the SWAT model, so that the geographical location of the meteorological stations after the downscaling of the HasGEM2-ES model data was the same as the location of the meteorological stations used in the SWAT model. The downscaling software CCT_Package (Vaghefi et al. 2017) was used to obtain the HasGEM2-ES model data with the same locations as the SWAT model meteorological stations. These data were then used for monthly statistics to obtain the average monthly precipitation, maximum temperature and minimum temperature of the HasGEM2-ES model for the historical period. The data were compared and corrected with SWAT model weather station data.

Handling of results

The simulation scale of the SWAT model for the MRBFPA is the monthly scale. The output file representing HRU in the model was exported to obtain the monthly HRU scale hydrological elements variation data for the period 1981–2015. The monthly-scale data were then interpolated using ArcGIS to obtain the $30\text{ m} \times 30\text{ m}$ resolution hydrological elements data for the MRBFPA over a 35 year period.

Results

Calibration and validation

This study began with a sensitivity analysis to identify the parameters that have a greater impact on the snowmelt runoff simulation. The sensitivity analysis was conducted by incorporating the Latin Hypercube sampling method (LH-OAT) into SWAT 2012. A parametric sensitivity analysis was conducted on common parameters, and those with high model sensitivity were selected for moderation. Table 2 shows the final selection of 16 parameters and their sensitivity and optimum values.

According to Table 2, basically all parameters are within the optimal range. The optimal value for the snowfall basal temperature (SFTMP) is 4.02, indicating that the transition from rain to snowfall begins at 4.02 °C. It is worth noting that the snowmelt basal temperature (SMTMP) is 4.64, indicating that snowmelt begins at 4.64 °C. The above model parameters are consistent with the findings of studies on snowfall events in and around the Tianshan Mountains (Yan and Jianli 2019) and snowmelt temperatures in the MRB (Gu et al. 2020; Xinchun et al. 2021). Other parameters such as hydraulic conductivity (SOL_K), SCS runoff curve coefficient (CN2) and slope (HRU_SLP) are given optimal values in the table above and the 16 hydrological parameters used are all within reasonable limits.

Table 1 SWAT model evaluation criteria (Moriasi et al. 2007)

| Performance grades | NSE | PBIAS |
|--------------------|---------------------------|------------------------|
| Very good | $1.00 \geq NSE \geq 0.75$ | $10 \geq PBIAS $ |
| Good | $0.75 > NSE \geq 0.65$ | $15 \geq PBIAS > 10$ |
| Satisfactory | $0.65 > NSE \geq 0.5$ | $25 \geq PBIAS > 15$ |
| Unsatisfactory | $0.5 > NSE$ | $ PBIAS > 25$ |

Table 2 Parameter selection and optimal value

| Parameter | Physical significance | Unit | Max value | Min value | Optimum value |
|------------------|---|----------------------|-----------|-----------|---------------|
| v__SMFMX.bsn | Maximum melt rate for snow during year | [mm/(°C day)] | 0 | 10 | 0.184 |
| v__SMFMN.bsn | Minimum melt rate for snow during year | [mm/(°C day)] | 0 | 10 | 0.075 |
| v__SFTMP.bsn | Snowfall temperature | [°C] | -5 | 5 | 4.022 |
| v__SMTMP.bsn | Snowmelt base temperature | [°C] | -5 | 5 | 4.640 |
| v__ESCO.bsn | Soil evaporation compensation factor | / | 0 | 1 | 0.824 |
| v__ALPHA_BF.gw | Baseflow alpha factor | [days] | 0 | 1 | 0.907 |
| v__GW_DELAY.gw | Groundwater delay | [days] | 0 | 500 | 161.420 |
| v__GWQMN.gw | Threshold depth of water required in shallow aquifer for return flow to occur | [mm] | 0 | 5000 | 329.107 |
| v__RCHRG_DP.gw | Deep aquifer percolation fraction | [fraction] | 0 | 1 | 0.262 |
| v__SLSUBBSN.hru | Average slope length | [m] | 10 | 150 | 1.328 |
| v__OV_N.hru | Manning's "n" value for overland flow | Na | 0.01 | 30 | 0.348 |
| v__HRU_SLP.hru | Average slope steepness | [m/m] | 0 | 0.6 | 0.248 |
| v__SOL_BD().sol | Moist bulk density | [g/cm ³] | 0.9 | 2.5 | 2.123 |
| v__SOL_K().sol | Saturated hydraulic conductivity | [mm/hr] | 0 | 2000 | 27.969 |
| v__SOL_AWC().sol | Available water capacity of the soil layer | [mm/mm] | 0 | 1 | 0.746 |
| v__TLAPS.sub | Temperature laps rate | [°C/km] | -50 | 50 | -5.180 |

R multiplies the existing value with (1 + the given value); V replaces the exiting value with the given value

Hydrological elements

Based on the results of the model rate determination, the results of the 35-year simulation of the SWAT model were used to analyse the hydrological elements in the MRBFPA. This section focuses on the monthly runoff, potential evapotranspiration (PET), actual evapotranspiration (ET), soil water content (SW) and snowmelt in the basin at the Kenswat hydrological station.

Runoff

Surface runoff simulations were conducted in the MRBFPA from 1979 to 2015. 1981–1999 data were used for rate calibration and 2000–2015 data for validation. This study set a warm-up time of two years (1979–1980) to initialize SWAT. The hydrological model of the MRBFPA was calibrated and compared with measured monthly runoff from 1981 to 2015 at the Kenswat hydrological station. Overall, the SWAT model simulated runoff had similar trends to the measured runoff, and the timing of flood occurrence between simulated and measured runoff information matched well. Figure 4 shows the results of the monthly-scale model simulated runoff.

From Fig. 4, the intra-annual runoff abundance pattern of the Manas River in the monthly-scale simulations varies significantly. The Manas River has a low flow rate in winter and a high flow rate in summer. Snowmelt accounts for 46% of the Manas River's annual runoff (Song Jinli and Yang Dewen, 2011). The low winter temperatures in the

MRBFPA cause the melting of snow and ice to stop. During the winter the recharge of snow and ice melt water to the runoff becomes low, resulting in significant seasonal variations in the Manas River runoff. As the temperature picks up, the rate of ice and snow melt increases and runoff increases rapidly. This is consistent with the more sensitive results for snow melt base temperature (SMTMP) from the parameter sensitivity analysis.

Table 3 shows the performance of the monthly-scale evaluation indicators of the SWAT hydrological model in the MRBFPA for the rate period (1981–1999) and the validation period (2000–2015), respectively.

As can be seen from Table 3, in the monthly-scale simulation calibration, for the rate period (1981–2000): NSE = 0.86, $R^2 = 0.87$, PBIAS = 13.75; for the validation period (2001–2015), NSE = 0.75, $R^2 = 0.77$, PBIAS = -11.78; and overall (1981–2015), NSE = 0.81, $R^2 = 0.81$, PBIAS = 1.44. Overall, in the monthly-scale simulations, the three performance parameters (NSE, R^2 and PBIAS) indicated very good simulation results during both the rate and validation periods, based on the performance evaluation criteria given in Table 1 and combined with the performance of the statistical indicators in Table 3.

Potential evapotranspiration (PET)

The potential evapotranspiration in the MRBFPA fluctuates between 180 and 330 mm over the 30 year period (Fig. 5). The potential evapotranspiration in the basin has generally declined over the period 1981–2007 and increased over the

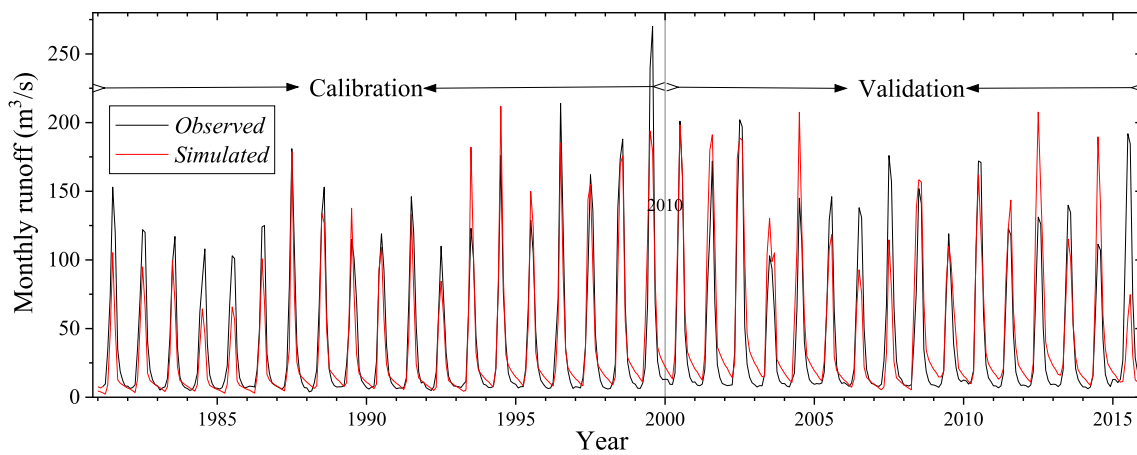


Fig. 4 Monthly runoff observed and simulated at Kenswat hydrological station

Table 3 The evaluation index value of periodic rate and validation period

| Statistical indicators | Calibration (1981–2000) | Validation (2001–2015) | Overall (1981–2015) |
|------------------------|-------------------------|------------------------|---------------------|
| NSE | 0.86 | 0.75 | 0.81 |
| R ² | 0.87 | 0.77 | 0.81 |
| PBIAS | 13.75 | −11.78 | 1.44 |

period 2008–2015, reaching a 30 year low of 186.23 mm in 2007 and a 30-year high of 325.49 mm in 1991. The interannual variation is within 30%. Based on the HRU distribution map, a PET value of HRU was assigned every 5 years to characterize the distribution and variation of potential evapotranspiration in the MRBFPA. As shown in Fig. 5, the PET changes were obtained every 5 years during 1981–2015 based on 747 HRU month-by-month PETs from 1981 to 2015 in the MRBFPA, where Ave (1981–2015) represents the 30-year average value of PET in the MRBFPA. Spatially, the annual PET in some areas of the basin can reach 1400 mm, while in lower areas the annual potential evapotranspiration is less than 100 mm. The spatial distribution of potential evapotranspiration is relatively stable with interannual climate change, and fluctuates with climate change in time.

Evapotranspiration (ET)

The ET in the MRBFPA fluctuated between 90 and 160 mm over the 30 years. Overall, the basin ET fluctuates around 130 mm, with interannual variation within 24%. There is a high degree of consistency between ET and PET variability in the MRBFPA. Based on the distribution map of HRU, the PET assignment of HRU was carried out every 5 years to characterize the distribution and variation of

evapotranspiration in the MRBFPA. As shown in Fig. 6, the month-by-month ET of 747 HRUs from 1981 to 2015 was calculated to obtain the change in ET for every 5 years between 1981 and 2015 in the MRBFPA, where Ave (1981–2015) represents the 30-year average evapotranspiration values. Spatially, the annual evapotranspiration in some areas of the basin is nearly 1000 mm, while in lower areas it is less than 50 mm, with significant spatial differences in evapotranspiration in the MRBFPA. With interannual climate change, the spatial distribution of actual evapotranspiration is relatively stable, fluctuating in time with climate change, and the fluctuations in evapotranspiration and potential evapotranspiration are highly similar (Fig. 5 and 6).

Soil water (SW)

The soil water content in the MRBFPA fluctuated between 32 and 42 mm over the 30 year period, with a general upward trend between 1981 and 2015. The interannual variability is within 17% and is less consistent with the ET and PET variability in the MRBFPA. Based on the HRU distribution map (Fig. 3), SW values of HRU were assigned every 5 years to characterize the distribution and variability of soil water content in the MRBFPA.

As shown in Fig. 7, the SW variation was calculated based on 747 HRU month-by-month SWs from 1981 to 2015 in the MRBFPA to obtain the SW variation every 5 years from 1981 to 2015, where Ave (1981–2015) represents the 30-year average soil water content values in the MRBFPA. The annual soil water content is about 85 mm in some areas of the basin and less than 20 mm in the lower areas, with significant spatial variation in evapotranspiration in the MRBFPA. Spatially, the areas with higher soil water content in the basin are downstream and at lower elevations. With interannual climate change, the spatial distribution is more stable and the soil water content then fluctuates significantly.

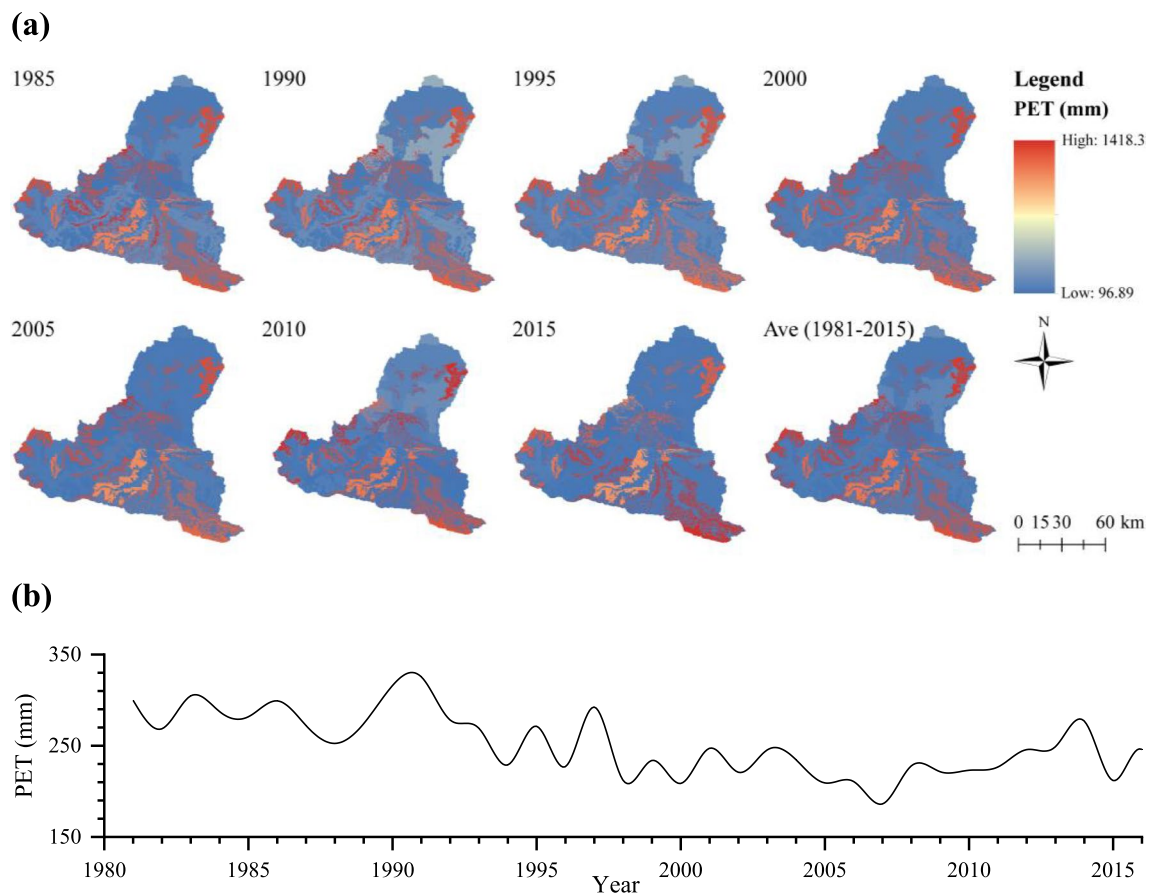


Fig. 5 PET (mm) in the MRBFPA, 1981–2015 **a** spatial distribution; **b** year-to-year variation

Snowmelt

Snowmelt (mm) in the MRBFPA from 1981 to 2015. The lowest value of snowmelt (mm) during the 30 year period was 21.64 mm in 2007 and the highest value of 106.94 mm in 2008. The difference in meltwater between 2007 and 2008 was 5 times. The interannual fluctuations in snow and ice melt water in the MRBFPA are in good agreement with the ET and PET variations in the basin production area, taking into account the fluctuations in temperature input that lead to a significant correlation between the three fluctuations. Snowmelt assignments of HRU were made every 5 years to characterize the spatial distribution and variability of snow and ice meltwater in the MRBFPA, based on the distribution map of HRU (Fig. 3). As shown in Fig. 8, the month-by-month Snowmelt of 747 HRUs from 1981 to 2015 was calculated to obtain the change in Snowmelt every 5 years during 1981–2015 in the MRBFPA, where Ave (1981–2015) denotes the 30-year average snow and ice meltwater values. The annual snow and ice melt water varies considerably between HRUs in the basin, with the highest annual snow melt up to 132 mm and the lowest up to 2.27 mm. In general, the spatial distribution of snow and ice melt water in the

basin fluctuates considerably between years, probably due to the combined effect of seasonal snow accumulation and temperature in the basin.

Runoff simulation under four scenarios

Runoff simulations for the MRBFPA based on four main climate change scenarios, RCP 2.6, 4.5, 6.0 and 8.5. Firstly, the runoff simulations for the four climate change scenarios for the Manas River from 2000 to 2020 were exported based on the available information, where 2000–2005 is the historical period, 2006–2020 is the simulated value under the four climate change scenarios, and the flow of the measured runoff is from 2000 to 2016, the results are shown in Fig. 9.

From 2000 to 2005, the historical data from the HadGEM2-ES model simulated the runoff in the MRBFPA relatively well. The simulated values of summer flows in 2000, 2002, 2003 and 2005 were slightly higher than the measured values; the simulated values of summer flows in 2001 and 2004 were slightly lower than the measured values.

From 2006 to 2016, a comparison of the simulated and measured values for the four climate change scenarios (RCP 2.6, 4.5, 6.0 and 8.5) of the HadGEM2-ES model

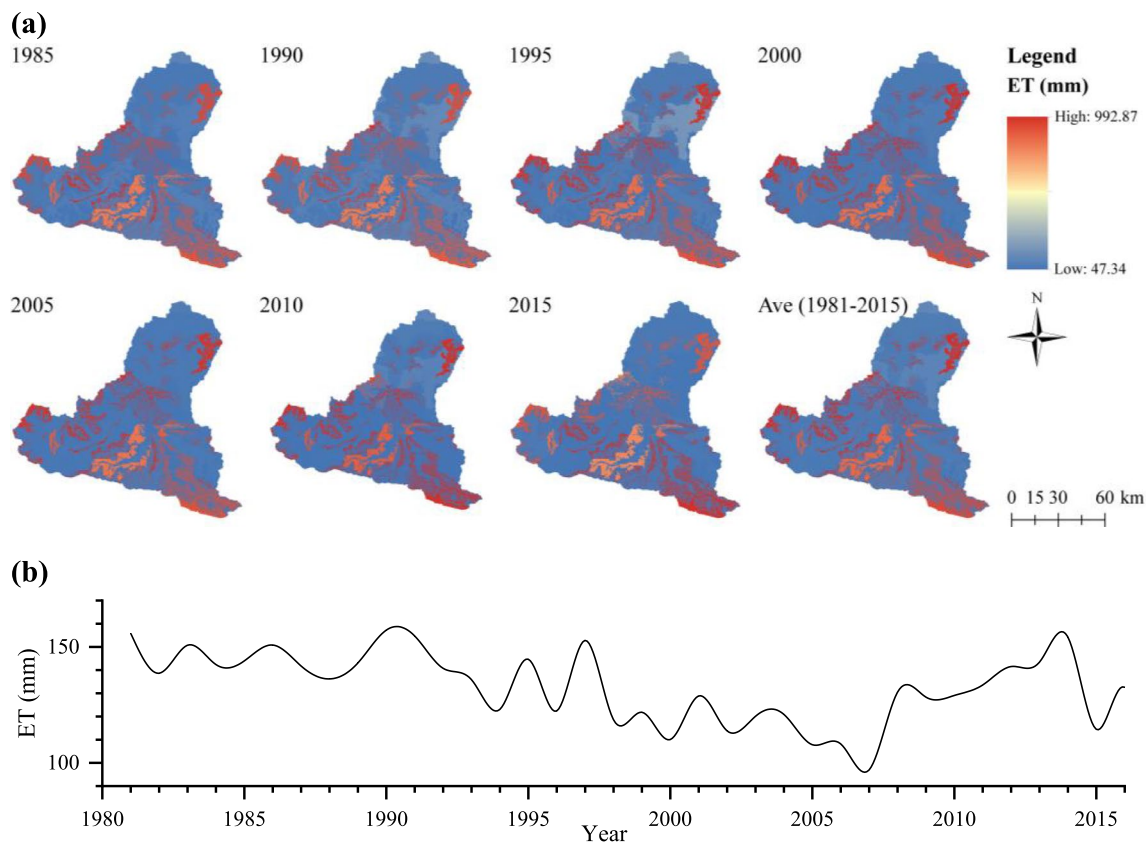


Fig. 6 ET (mm) in the MRBFPA, 1981–2015 **a** spatial distribution; **b** year-to-year variation

showed that the measured runoff flow in the MRBFPA was between the simulated values for the RCP 6.0 and RCP 8.5 scenarios. Further work is needed to verify the strengths and weaknesses of the modelled and measured values under the four climate change scenarios.

A detailed comparison of the simulated and measured values for 2006–2016 under RCP 6.0 and RCP 8.5 scenarios (Fig. 10) shows that the difference between the measured runoff and the simulated flow under the RCP 8.5 scenario for these 11 years is minimal. The simulated and measured values under the four climate change scenarios were then validated using the criteria in Table 1 to analyse the trends in climate change in the MRBFPA, and the results are shown in Table 4.

As can be seen from the above table, the simulated and measured runoff values for the RCP 8.5 climate change scenario are closest to each other for the period 2006–2016, with $NSE = 0.7$, $R^2 = 0.80$ and $PBIAS = 4.80$, all three performance parameters meet the very good criteria in Table 1. Based on the analysis of the above results, it can be concluded that climate change in the MRBFPA during 2006–2016 is close to the RCP 8.5 climate change scenario due to the effects of global warming (Alvarenga et al. 2015).

Water resources available

Water resources in the MRBFPA are pooled in the Kenswat reservoir, which is then dispatched in a unified manner to allocate total water resources within the year according to midstream irrigation demand. This sub-section assesses the future total water resources in the MRB for the period 2020–2099, providing a basis for the rational use of water resources in the basin, annual allocation and interannual arable land planning. The future total annual-scale water resources in the MRBFPA are calculated based on the modelled values of each of the four climate change scenarios.

The measured runoff lies between the modelled values for the RCP 6.0 and RCP 8.5 climate change scenarios and is closer to the modelled values for the RCP 8.5 scenario. 2021–2025 has an annual average water volume of around $13.0 \times 10^8 \text{ m}^3$. 2026–2030 has an annual average water volume of around $15.0 \times 10^8 \text{ m}^3$. 2021–2025 is a dry year. The average annual water inflow from Kenswat Reservoir increases from 2026 to 2030; the water inflow from Kenswat Reservoir increases with a high probability and decreases with a low probability from 2031 to 2035, and the five-year average annual water volume is between 14.0×10^8 and $16.0 \times 10^8 \text{ m}^3$.

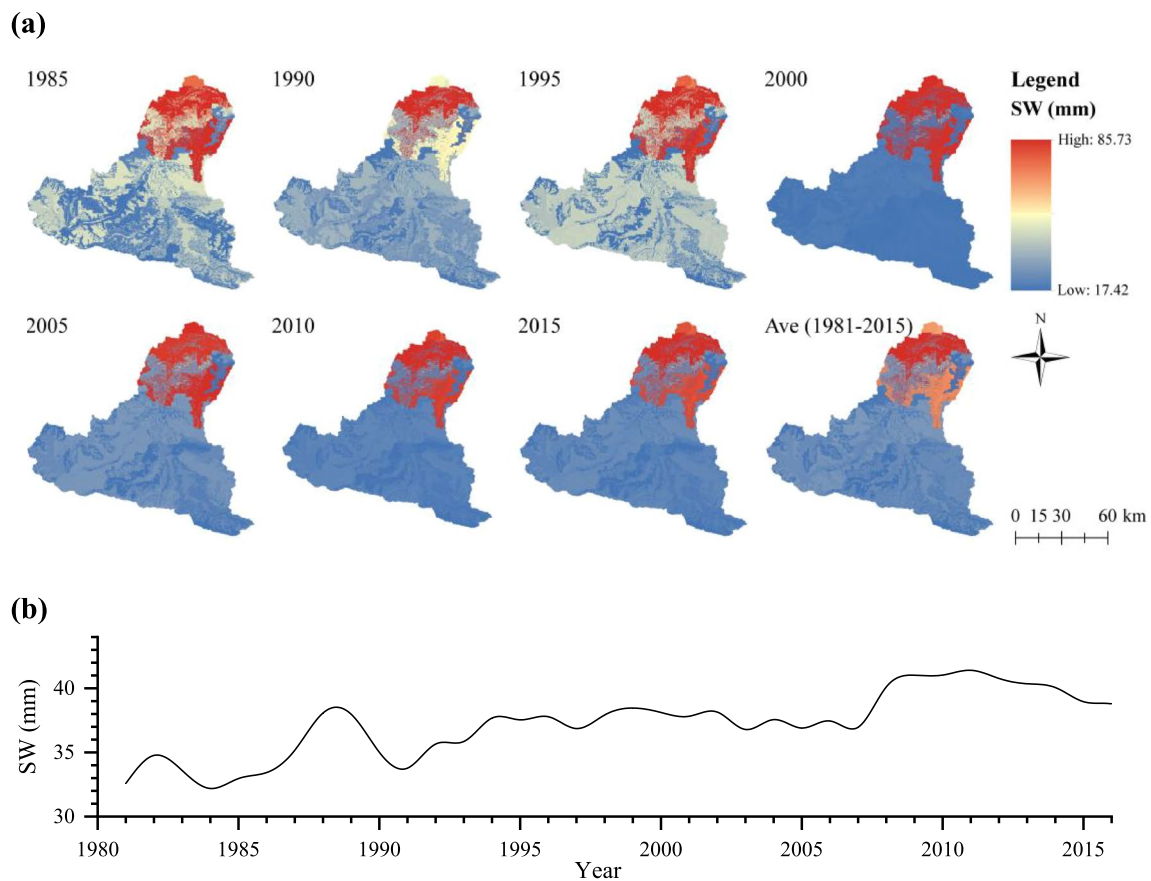


Fig. 7 SW (mm) in the MRBFPA, 1981–2015 **a** spatial distribution; **b** year-to-year variation

Calculating the average annual water resources in the MRBFPA from 2020 to 2099 under the four climate change scenarios revealed that the total average annual water resources in the MRBFPA under the RCP 2.6, 4.5, 6.0 and 8.5 climate change scenarios were $14.21 \times 10^8 \text{ m}^3$, $13.56 \times 10^8 \text{ m}^3$, $13.09 \times 10^8 \text{ m}^3$ and $13.44 \times 10^8 \text{ m}^3$ Table (5).

According to the results of the analysis in Fig. 10, climate change in the MRBFPA is close to the RCP 8.5 climate change scenario. Considering that the current climate change scenario remains unchanged, and taking into account that the basin flow-producing areas undergo interannual adjustment of water resources, the SWAT hydrological model outputs under the RCP 8.5 climate change scenario were used to calculate the total water resources in the MRBFPA, and the results are shown in Fig. 11.

The average annual water resources in the MRBFPA is $12.95 \times 10^8 \text{ m}^3$. Under the RCP 8.5 climate change scenario, the total water resources in the MRBFPA fluctuate around $12.95 \times 10^8 \text{ m}^3$ between 2020 and 2099, with the water resources in 2028 being as high as $23.08 \times 10^8 \text{ m}^3$, higher than the average annual water resources in the MRBFPA of $12.95 \times 10^8 \text{ m}^3$; the water resources in 2060 are as low as $6.59 \times 10^8 \text{ m}^3$, much lower than the average

annual water resources in the MRBFPA. Between 2027 and 2036, the water resources in the MRBFPA were more than $12.95 \times 10^8 \text{ m}^3$, and between 2067 and 2078, the water resources in the MRBFPA were less than $12.95 \times 10^8 \text{ m}^3$. Runoff in the MRBFPA is strongly influenced by climate change.

Discussion

In the last 40 years, the area of artificial oases in the oasis zone of the MRB has expanded by 129.56% due to the booming development of water-saving irrigation (Zhang 2018; Liao et al. 2020), and the socioeconomic effects works on the oases have positively contributed to the development of the region (Yang et al. 2017). However, at the same time, the demand for water in the MRB is increasing (Gu et al. 2020; Liao et al. 2021). Water resources analysis and modelling of the basin is the basis of water resources control and a prerequisite for sustainable regional development (Gupta et al. 1999; Yaning et al. 2012; Baffaut et al. 2015; Cao et al. 2018). In this paper, we used ArcSWAT 2012 to classify the MRBFPA into 19 sub-basins and 747

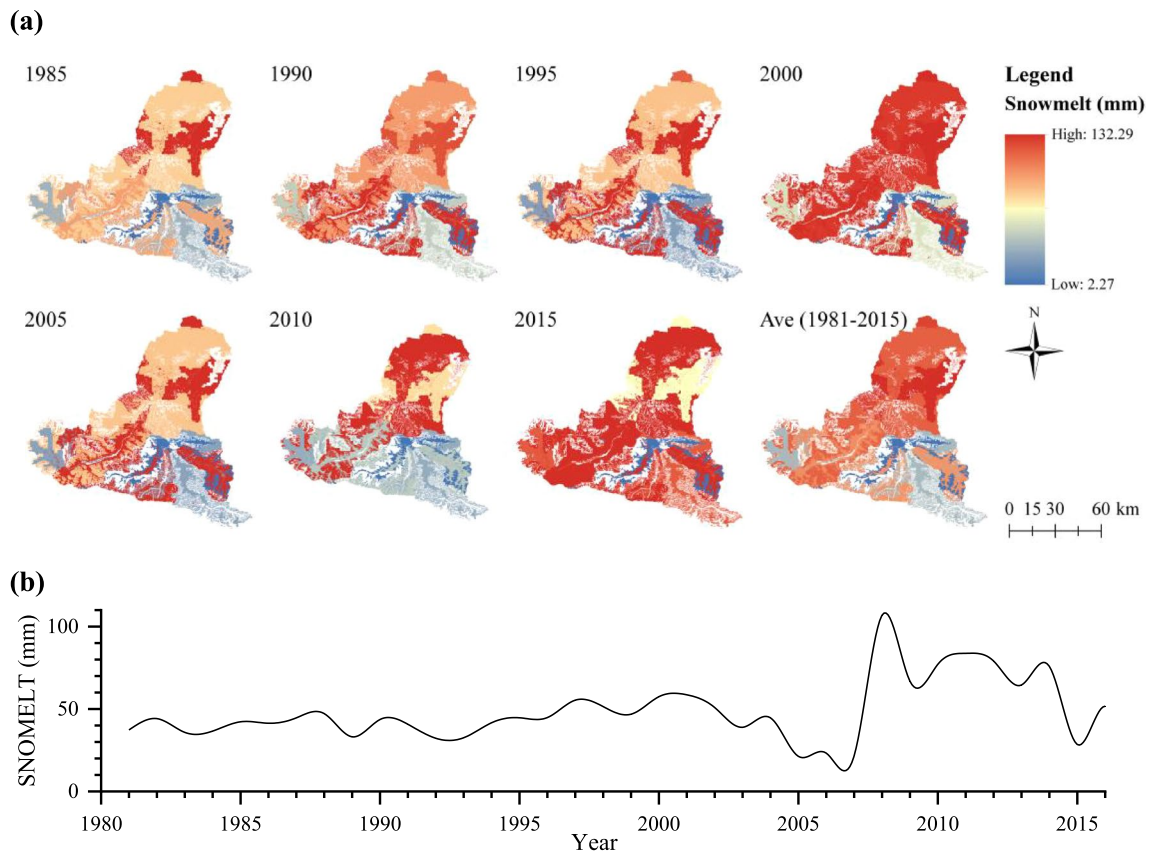


Fig. 8 Snowmelt (mm) in the MRBFPA, 1981–2015 a spatial distribution; b year-to-year variation

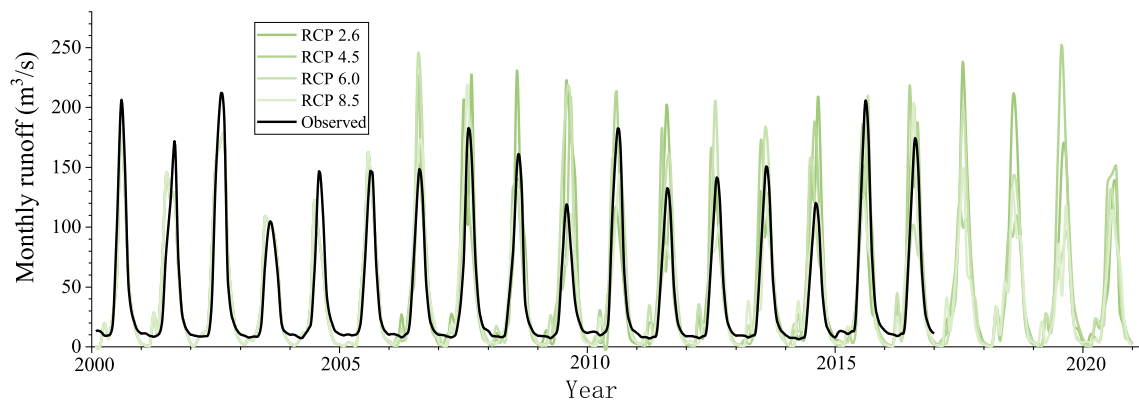


Fig. 9 Response of runoff to four scenarios in MRBFPA from 2000 to 2020

HRUs and conducted rate determination and validation. For the rate determination period (1981–1999): $NSE=0.86$, $R^2=0.87$, $PBIAS=13.75$; for the validation period (2000–2015), $NSE=0.75$, $R^2=0.77$, $PBIAS=-11.78$; overall (1981–2015), $NSE=0.81$, $R^2=0.81$, $PBIAS=1.44$. The optimal value for snowmelt base temperature (SMTMP) was 4.64 and the optimal value for snowfall base temperature (SFTMP) was 4.02, indicating that the snow-water transition

temperature in the MRB was around $4\text{ }^\circ\text{C}$, which is consistent with previous studies that snowfall events in and around the Tianshan Mountains largely occurred between $-35\text{ }^\circ\text{C}$ and $5\text{ }^\circ\text{C}$ (Yan and Jianli 2019; Gu et al. 2020; Xinchen et al. 2021).

Based on the SWAT model, the changes of hydrological elements (runoff, potential evapotranspiration, actual evapotranspiration, soil water content, snow and ice ablation) in

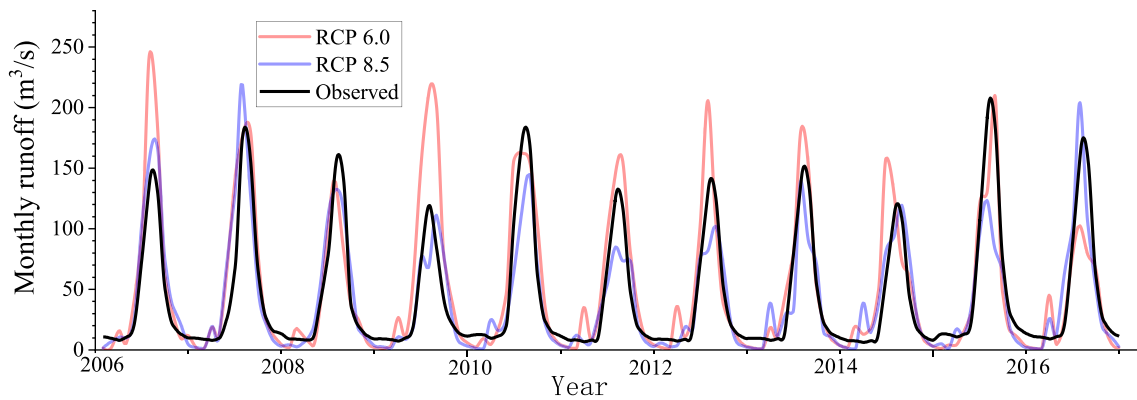


Fig. 10 Flow simulation of Manas River for 2006–2016 under RCP 6.0 and RCP 8.5 scenarios

Table 4 Evaluation of simulation effect under different climate change scenarios

| Scenarios | NSE | R ² | PBIAS |
|----------------------|------|----------------|--------|
| RCP 2.6 ^c | 0.55 | 0.67 | -10.89 |
| RCP 4.5 ^c | 0.63 | 0.74 | -9.92 |
| RCP 6.0 ^b | 0.67 | 0.78 | -16.40 |
| RCP 8.5 ^a | 0.79 | 0.80 | 4.80 |

a, b, c denote the classification criteria in Table 1, where a represents very good, b represents good, and c represents satisfactory

Table 5 Water resources of annual runoff area in 2020–2099 under different climate change scenarios

| Scenarios | RCP 2.6 | RCP 4.5 | RCP 6.0 | RCP 8.5 |
|---|---------|---------|---------|---------|
| Water resources (10 ⁸ m ³) | 14.21 | 13.56 | 13.09 | 13.44 |

the MRBFPA were analysed. The results show that evapotranspiration in the MRBFPA fluctuated between 90 and 160 mm over the 30-year period. The lowest value of basin

evapotranspiration in the 30-year period was 97.00 mm in 2007 and the highest value of 157.23 mm in 1990. The interannual variation is within 24%. Soil water content in the MRBFPA fluctuates between 32 and 42 mm, with a general upward trend between 1981 and 2015. The interannual variation is within 17%. The snow and ice melt water in the MRBFPA fluctuates between 32 and 42 mm. In 2007, the lowest value of snow and ice melt water in the basin in 30 years was 21.64 mm and in 2008 the highest value of 106.94 mm. Overall, there are large fluctuations in snow and ice melt water in the basin (Luo et al. 2012, 2013). The fluctuations in interannual snow and ice melt water in the basin production area are in good agreement with the changes in ET and PET in the basin production area, which is considered to be a significant correlation between the fluctuations in temperature input and the fluctuations in the three.

The maximum and minimum temperature estimates in HasGEM2-ES model are in good agreement with the available basin meteorological data (Jones et al. 2011; Gu et al. 2020), while the precipitation estimates vary considerably, especially for the months of June to August. The meteorological data provided by the HadGEM2-ES model

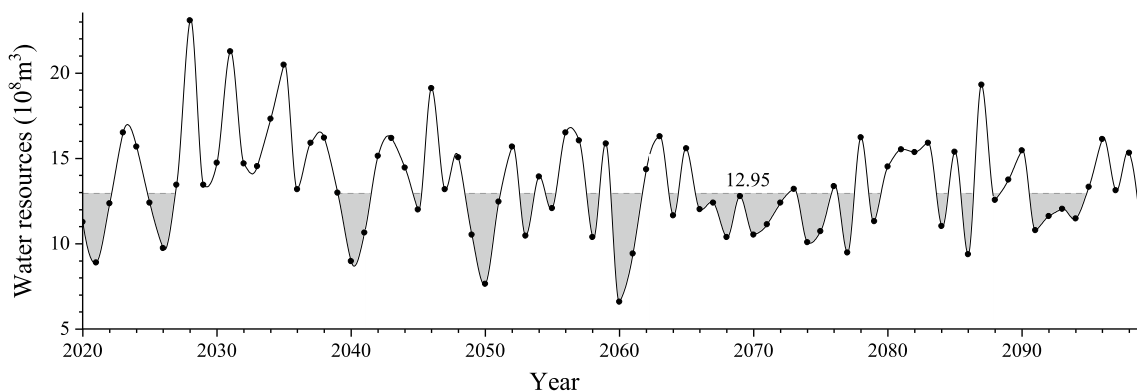


Fig. 11 Total water resources of runoff producing areas in 2020–2099 under RCP 8.5 scenario

underestimate the precipitation in the MRB for the months of June and August (Song Jinli and Yang Dewen, 2011). We obtained meteorological data for different future scenarios consistent with the flow-producing areas of the MRB by correcting the HasGEM2-ES data (AF1). The total future available water resources in the basin were estimated accordingly, and it was found that the climate change scenario for the MRB is close to the RCP8.5 discharge scenario.

Hydrological uncertainty in the MRBFPA is further enhanced under the climate change scenario of RCP 8.5, this is in line with previous studies (Guo and Shen 2016). The total multi-year average water resources in the MRBFPA between 1956 and 2015 was $12.95 \times 10^8 \text{ m}^3$, with a minimum value of $9.53 \times 10^8 \text{ m}^3$ reached in 1957 and a maximum value of $19.87 \times 10^8 \text{ m}^3$ reached in 1999. Historical interannual water resources fluctuate between 73.59 and 153.44% of the multi-year average water resources. The interannual fluctuations in total water resources in the MRBFPA between 2020 and 2099 under the RCP 8.5 climate change scenario increase further, reaching a maximum value of $23.08 \times 10^8 \text{ m}^3$ in 2028 and a minimum value of $6.59 \times 10^8 \text{ m}^3$ in 2060, with interannual variability over the next 80 years ranging from between 50.89 and 178.22%.

Conclusions

This study constructed a SWAT model for MRBFPA and estimated the water resources in MRBFPA based on HadGEM2-ES. The results showed that:

1. The fluctuations in PET, ET, SW and Snowmelt in MRBFPA have further intensified in the past two decades.
2. The climate change scenario in MRBFPA is close to RCP 8.5, and the uncertainty of water resources and extreme hydrological conditions will further intensify in the future.
3. The water resources of MRBFPA reached its maximum value of $23.08 \times 10^8 \text{ m}^3$ in 2028, reaching a minimum value of $6.59 \times 10^8 \text{ m}^3$ in 2060. The interannual variability for the next 80 years is between 50.89 and 178.22%.

The northern slopes of the Tianshan Mountains are an industrial concentration in the Xinjiang region, but the socio-economic development of the region is limited by water resources that are dominated by glacial meltwater. Understanding and addressing the relationship between climate change and water resources is a prerequisite for the region's development. We believe that monitoring of glaciers and meteorology in the MRBFPA should be strengthened to improve the ability to respond to climate change and the sustainable development of the basin should be supported.

Appendix

See Table 6

Table 6 SWAT model soil database of MRBFPA

| Objectid | MUID | SEQN | SNAM | S5ID | CMPPT | NLAYERS | HYDGRP | SOL_ZMX | ANION_ EXCL | SOL_CRK | TEXTURE | | |
|----------|----------|---------|-----------|-----------|-----------|-----------|--------|---------|-------------|-----------|-----------|----------|----------|
| 11103 | 0 | 0 | GRh | 0 | 1 | 2 | A | 1000 | 0.5 | 0 | 0 | | |
| 11120 | 0 | 0 | CHh | 0 | 1 | 2 | A | 1000 | 0.5 | 0 | 0 | | |
| 11145 | 0 | 0 | KSI | 0 | 1 | 2 | C | 1000 | 0.5 | 0 | 0 | | |
| 11158 | 0 | 0 | KSh | 0 | 1 | 2 | A | 1000 | 0.5 | 0 | 0 | | |
| 11173 | 0 | 0 | KSk | 0 | 1 | 2 | A | 1000 | 0.5 | 0 | 0 | | |
| 11341 | 0 | 0 | FLc | 0 | 1 | 2 | C | 1000 | 0.5 | 0 | 0 | | |
| 11705 | 0 | 0 | LPi | 0 | 1 | 2 | D | 300 | 0.5 | 0 | 0 | | |
| 11724 | 0 | 0 | LPm | 0 | 1 | 2 | D | 300 | 0.5 | 0 | 0 | | |
| 11765 | 0 | 0 | LPi | 0 | 1 | 2 | D | 300 | 0.5 | 0 | 0 | | |
| 11930 | 0 | 0 | GG | 0 | 1 | 2 | A | 300 | 0.5 | 0 | 0 | | |
| Objectid | SOL_Z1 | SOL_BD1 | SOL_ AWC1 | SOL_K1 | SOL_ CBN1 | CLAY1 | SILT1 | SAND1 | ROCK1 | SOL_ ALB1 | USLE_K1 | SOL_EC1 | |
| 11103 | 300 | 1.23 | 18.3 | 24.11 | 1.6 | 21 | 54 | 25 | 0 | 0.01 | 0.05403 | 0 | |
| 11120 | 300 | 1.17 | 18.6 | 26.18 | 2.09 | 23 | 54 | 23 | 0 | 0.01 | 0.053728 | 0 | |
| 11145 | 300 | 1.3 | 15.8 | 22.81 | 1.28 | 22 | 42 | 36 | 0 | 0.01 | 0.047865 | 0 | |
| 11158 | 300 | 1.31 | 15.6 | 23.67 | 1.2 | 21 | 42 | 37 | 0 | 0.01 | 0.048326 | 0 | |
| 11173 | 300 | 1.26 | 16.5 | 17.67 | 1.42 | 26 | 45 | 29 | 0 | 0.01 | 0.048638 | 0 | |
| 11341 | 300 | 1.38 | 16.2 | 22.29 | 0.6 | 18 | 48 | 34 | 0 | 0.01 | 0.062615 | 0 | |
| 11705 | 300 | 1.3 | 13.3 | 88.45 | 1.41 | 6 | 38 | 56 | 0 | 0.01 | 0.05942 | 0 | |
| 11724 | 300 | 1.1 | 17.6 | 42.65 | 3.02 | 20 | 45 | 35 | 0 | 0.01 | 0.049284 | 0 | |
| 11765 | 300 | 1.3 | 13.3 | 88.45 | 1.41 | 6 | 38 | 56 | 0 | 0.01 | 0.05942 | 0 | |
| 11930 | 300 | 1.53 | 27.1 | 13.56 | 0 | 0 | 0 | 0 | 0 | 0.01 | 0.49999 | 0 | |
| Objectid | SOL_ EC1 | SOL_Z2 | SOL_ BD2 | SOL_ AWC2 | SOL_K2 | SOL_ CBN2 | CLAY2 | SILT2 | SAND2 | ROCK2 | SOL_ ALB2 | USLE_ K2 | SOL_ EC2 |
| 11103 | 0 | 700 | 1.34 | 16.7 | 9.88 | 0.4 | 28 | 49 | 23 | 0 | 0.01 | 0.065626 | 0 |
| 11120 | 0 | 700 | 1.32 | 17.4 | 17.5 | 0.89 | 22 | 52 | 26 | 0 | 0.01 | 0.056616 | 0 |
| 11145 | 0 | 700 | 1.34 | 15.6 | 11.75 | 0.6 | 28 | 42 | 30 | 0 | 0.01 | 0.057157 | 0 |
| 11158 | 0 | 700 | 1.39 | 15.2 | 20.09 | 0.48 | 20 | 43 | 37 | 0 | 0.01 | 0.061423 | 0 |
| 11173 | 0 | 700 | 1.35 | 16.3 | 14.23 | 0.57 | 24 | 47 | 29 | 0 | 0.01 | 0.061199 | 0 |
| 11341 | 0 | 700 | 1.41 | 15.6 | 21.36 | 0.4 | 18 | 46 | 36 | 0 | 0.01 | 0.065255 | 0 |
| 11705 | 0 | 0 | 1.53 | 27.1 | 13.56 | 0 | 0 | 0 | 0 | 0 | 0.01 | 0.5 | 0 |
| 11724 | 0 | 0 | 1.53 | 27.1 | 13.56 | 0 | 0 | 0 | 0 | 0 | 0.01 | 0.5 | 0 |
| 11765 | 0 | 0 | 1.53 | 27.1 | 13.56 | 0 | 0 | 0 | 0 | 0 | 0.01 | 0.5 | 0 |
| 11930 | 0 | 0 | 1.53 | 27.1 | 13.56 | 0 | 0 | 0 | 0 | 0 | 0.01 | 0.5 | 0 |

Author contributions XG and AL contributed to conceptualization; NP, HY and HL contributed to data curation, resources and formal analysis; HW and AL performed investigation; XG and XL provided methodology; XG performed writing—original draft preparation; XG and HW performed writing—review; HW and XG revised the manuscript; AL and XH performed supervision.

Funding This research was supported by the Third Xinjiang Scientific Expedition Program (Grant Number: 2021XJJK0400); Xinjiang Production and Construction Corps (Grant Number: 2021AB021) and the National Natural Science Foundation of China (Grant Number: 52379020).

Declarations

Conflict of interest The authors declare that they have no known competing financial interests or personal relationships that could have appeared to influence the work reported in this paper.

Open Access This article is licensed under a Creative Commons Attribution 4.0 International License, which permits use, sharing, adaptation, distribution and reproduction in any medium or format, as long as you give appropriate credit to the original author(s) and the source, provide a link to the Creative Commons licence, and indicate if changes were made. The images or other third party material in this article are included in the article's Creative Commons licence, unless indicated otherwise in a credit line to the material. If material is not

included in the article's Creative Commons licence and your intended use is not permitted by statutory regulation or exceeds the permitted use, you will need to obtain permission directly from the copyright holder. To view a copy of this licence, visit <http://creativecommons.org/licenses/by/4.0/>.

References

- Abbaspour KC, Yang J, Maximov I, Siber R, Bogner K, Mieleitner J, Zobrist J, Srinivasan R (2007) Modelling hydrology and water quality in the pre-alpine/alpine thur watershed using SWAT. *J Hydrol* 333(2–4):413–430
- Agr S (1980) CREAMS: a field scale model for chemicals, runoff, and erosion from agricultural management systems. Conservation Research Report No 26
- Alvarenga RAF, Erb K-H, Haberl H, Soares SR, van Zelm R, Dewulf J (2015) Global land use impacts on biomass production—a spatial-differentiated resource-related life cycle impact assessment method. *Int J Life Cycle Assess* 20(4):440–450
- Arnold JG, Allen PM, Volk M, Williams JR, Bosch DD (2010) Assessment of different representations of spatial variability on SWAT model performance. *Trans ASABE* 53(5):1433–1443
- Arnold JG, Moriasi DN, Gassman PW, Abbaspour KC, White MJ, Srinivasan R, Santhi C, Harmel RD, van Griensven A, van Liew MW, Kannan N, Jha MK (2012) SWAT: model use, calibration, and validation. *Trans ASABE* 55(4):1491–1508
- Baffaut C, Sadler EJ, Ghidry F, Anderson SH (2015) Long-term agroecosystem research in the central Mississippi river basin SWAT simulation of flow and water quality in the Goodwater creek experimental watershed. *J Environ Qual* 44(1):84–96
- Boughton WC (1989) A review of the USDA SCS curve number method. *Aust J Soil Res* 27(3):511–523
- Cao Y, Zhang J, Yang M, Lei X, Guo B, Yang L, Zeng Z, Qu J (2018) Application of SWAT model with CMADS data to estimate hydrological elements and parameter uncertainty based on SUFI-2 algorithm in the Lijiang river basin, China. *Water* 10(6):742
- Center on Climate Change, CMA (2020) Blue book on climate change in China 2020. Science Press, Beijing
- Cheng B, Li H (2018) Agricultural economic losses caused by protection of the ecological basic flow of rivers. *J Hydrol* 564:68–75
- Cho KH, Pachepsky YA, Kim JH, Kim J-W, Park M-H (2012) The modified SWAT model for predicting fecal coliforms in the Wachusett reservoir watershed, USA. *Water Res* 46(15):4750–4760
- Frieler K, Lange S, Piontek F, Reyer CPO, Schewe J, Warszawski L, Zhao F, Chini L, Denvil S, Emanuel K, Geiger T, Halladay K, Hurtt G, Mengel M, Murakami D, Ostberg S, Popp A, Riva R, Stevanovic M, Suzuki T, Volkholz J, Burke E, Ciais P, Ebi K, Eddy TD, Elliott J, Galbraith E, Gosling SN, Hattermann F, Hickler T, Hinkel J, Hof C, Huber V, Jagermeyr J, Krysanova V, Marce R, Schmied HM, Mouratiadou I, Pierson D, Tittensor DP, Vautard R, van Vliet M, Biber MF, Betts RA, Bodirsky BL, Deryng D, Frolking S, Jones CD, Lotze HK, Lotze-Campen H, Sahajpal R, Thonicke K, Tian H, Yamagata Y (2017) Assessing the impacts of 1.5 degrees C global warming—simulation protocol of the inter-sectoral impact model intercomparison project (ISIMIP2b). *Geosci Model Dev* 10(12):4321–4345
- Geng Q, Wu P, Zhao X (2016) Spatial and temporal trends in climatic variables in arid areas of northwest China. *Int J Climatol* 36(12):4118–4129
- Ghaffari G, Keesstra S, Ghodousi J, Ahmadi H (2010) SWAT-simulated hydrological impact of land-use change in the Zanjanrood basin. *Northwest Iran Hydrol Process* 24(7):892–903
- Gu X, Yang G, He X, Zhao L, Li X, Li P, Liu B, Gao Y, Xue L, Long A (2020) Hydrological process simulation in Manas river basin using CMADS. *Open Geosciences* 12(1):946–957
- Gu X, Zhang P, Zhang W, Liu Y, Jiang P, Wang S, Lai X, Long A (2023) A study of drought and flood cycles in Xinyang, China, using the wavelet transform and M-K test. *Atmosphere* 14(8):1196
- Guglielmi G (2022) Climate change is turning more of central Asia into desert. *Nature*. <https://doi.org/10.1038/d41586-022-01667-2>
- Guo Y, Shen Y (2016) Agricultural water supply/demand changes under projected future climate change in the arid region of northwestern China. *J Hydrol* 540:257–273
- Gupta HV, Sorooshian S, Yapo PO (1999) Status of automatic calibration for hydrologic models: comparison with multilevel expert calibration. *J Hydrol Eng* 4(2):135–143
- Hargreaves GH, Allen RG (2003) History and evaluation of Hargreaves evapotranspiration equation. *J Irrig Drain Eng* 129(1):53–63
- Hargreaves G, Samani Z (1985) Reference crop evapotranspiration from temperature. *Appl Eng Agric* 1(2):96–99
- He H, Wang Z, Guo L, Zheng X, Zhang J, Li W, Fan B (2018) Distribution characteristics of residual film over a cotton field under long-term film mulching and drip irrigation in an oasis agroecosystem. *Soil Tillage Res* 180:194–203
- Hu Y, Duan W, Chen Y, Zou S, Kayumba PM, Sahu N (2021) An integrated assessment of runoff dynamics in the Amu Darya river basin: confronting climate change and multiple human activities, 1960–2017. *J Hydrol* 603:126905
- Igarashi T (2001) ALOS mission requirement and sensor specifications. *Adv Space Res* 28:127–131
- Intergovernmental Panel on Climate Change (2018) Special report on global warming of 1.5°C. Cambridge University Press, UK
- Jinli S, Dewen Y (2011) Characterization of water resources in the Manas river basin. *Inner Mongolia Water Resour* 04:109–110
- Jones CD, Hughes JK, Bellouin N, Hardiman SC, Jones GS, Knight J, Liddicoat S, O'Connor FM, Andres RJ, Bell C, Boo K-O, Bozzo A, Butchart N, Cadule P, Corbin KD, Doutriaux-Boucher M, Friedlingstein P, Gornall J, Gray L, Halloran PR, Hurtt G, Ingram WJ, Lamarque J-F, Law RM, Meinshausen M, Osprey S, Palin EJ, Chini LP, Raddatz T, Sanderson MG, Sellar AA, Schurer A, Valdes P, Wood N, Woodward S, Yoshioka M, Zerroukat M (2011) The HadGEM2-ES implementation of CMIP5 centennial simulations. *Geosci Model Dev* 4(3):543–570
- Kang S, Hao X, Du T, Tong L, Su X, Lu H, Li X, Huo Z, Li S, Ding R (2017) Improving agricultural water productivity to ensure food security in China under changing environment: from research to practice. *Agric Water Manag* 179:5–17
- Li X, Cheng G, Ge Y, Li H, Han F, Hu X, Tian W, Tian Y, Pan X, Nian Y, Zhang Y, Ran Y, Zheng Y, Gao B, Yang D, Zheng C, Wang X, Liu S, Cai X (2018a) Hydrological cycle in the Heihe river basin and its implication for water resource management in Endorheic basins. *J Geophys Res-Atmos* 123(2):890–914
- Li Y, Chen Y, Li Z, Fang G (2018b) Recent recovery of surface wind speed in northwest China. *Int J Climatol* 38(12):4445–4458
- Liao N, Gu X, Wang Y, Xu H, Fan Z (2020) Analyzing macro-level ecological change and micro-level farmer behavior in Manas river basin, China. *Land* 9(8):250
- Liao N, Gu X, Wang Y, Xu H, Fan Z (2021) Analysis of ecological and economic benefits of rural land integration in the Manas river basin Oasis. *Land* 10(5):451
- Ling H, Xu H, Fu J, Liu X (2012) Surface runoff processes and sustainable utilization of water resources in Manas river basin, Xinjiang, China. *J Arid Land* 4(3):271–280
- Liu B, Zhao W, Wen Z, Yang Y, Chang X, Yang Q, Meng Y, Liu C (2019) Mechanisms and feedbacks for evapotranspiration-induced

- salt accumulation and precipitation in an arid wetland of China. *J Hydrol* 568:403–415
- Luo Y, Arnold J, Allen P, Chen X (2012) Baseflow simulation using SWAT model in an inland river basin in Tianshan mountains Northwest China. *Hydrol Earth Syst Sci* 16(4):1259–1267
- Luo Y, Arnold J, Liu S, Wang X, Chen X (2013) Inclusion of glacier processes for distributed hydrological modeling at basin scale with application to a watershed in Tianshan mountains, northwest China. *J Hydrol* 477:72–85
- Mingjiang D (2018) "ThreeWater Lines" strategy: its spatial patterns and effects on water resources allocation in northwest China. *Acta Geogr Sin* 73(7):1189–1203
- Monteith JL (1965) Evaporation and environment. *Symp Soc Exp Biol* 19:205–234
- Moriiasi DN, Arnold JG, van Liew MW, Bingner RL, Harmel RD, Veith TL (2007) Model evaluation guidelines for systematic quantification of accuracy in watershed simulations. *Trans ASABE* 50(3):885–900
- Nash JE, Sutcliffe JV (1970) River flow forecasting through conceptual models part I—a discussion of principles. *J Hydrol* 10(3):282–290
- Pereira DDR, Martinez MA, Pruski FF, da Silva DD (2016) Hydrological simulation in a basin of typical tropical climate and soil using the SWAT model part I: calibration and validation tests. *J Hydrol Reg Stud* 7:14–37
- Priestley C, Taylor R (1972) On the assessment of surface heat flux and evaporation using large scale parameters. *Mwr* 100:81–92
- Qi J, Li S, Jamieson R, Hebb D, Xing Z, Meng F-R (2017) Modifying SWAT with an energy balance module to simulate snowmelt for maritime regions. *Environ Modell Softw* 93:146–160
- Sloan PG, Moore ID (1984) Modeling subsurface stormflow on steeply sloping forested watersheds. *Water Resour Res* 20(12):1815–1822
- Sorg A, Bolch T, Stoffel M et al (2012) Climate change impacts on glaciers and runoff in Tien Shan (Central Asia). *Nat Clim Change* 2:725–731
- Thomas A (2000) Spatial and temporal characteristics of potential evapotranspiration trends over China. *Int J Climatol* 20(4):381–396
- Tian Z, Ramsbottom D, Sun L et al (2023) Dynamic adaptive engineering pathways for mitigating flood risks in Shanghai with regret theory. *Nat Water* 1:198–208
- Vaghefi SA, Abbaspour N, Kamali B, Abbaspour KC (2017) A toolkit for climate change analysis and pattern recognition for extreme weather conditions: case study California-Baja California Peninsula. *Environ Modell Softw* 96:181–198
- Water Resources Department of the Ministry of Water Resources (2021) China water resources bulletin in 2020. China Water Conservancy and Hydropower Press, Beijing
- Williams AP, Cook BI, Smerdon JE (2022) Rapid intensification of the emerging southwestern North American megadrought in 2020–2021. *Nat Clim Chang* 12:232–234
- Xinchen G, Senyuan X, Guang Y, Xinlin H, Qi Z, Liang Z, Dongbo L (2021) Hydrological process simulation of Manas river basin based on CMADS and SWAT model. *J Water Resour Water Eng* 32(2):116–123
- Yan Q, Jianli D (2019) Change characteristics of different types of snowfall event in China's Tianshan mountains from 1961 to 2016. *Adv Water Sci* 30(4):457–466
- Yang G, Xue L, He X, Wang C, Long A (2017) Change in land use and evapotranspiration in the Manas river basin, China with long-term water-saving measures. *Sci Rep* 7(1):17874
- Yang G, Li F, Chen D, He X, Xue L, Long A (2019) Assessment of changes in oasis scale and water management in the arid Manas river basin, north western China. *Sci Total Environ* 691:506–515
- Yang G, Tian L, Li X, He X, Gao Y, Li F, Xue L, Li P (2020) Numerical assessment of the effect of water-saving irrigation on the water cycle at the Manas river basin oasis, China. *Sci Total Environ* 707:135587
- Yaning C, Qing Y, Yi L, Yanjun S, Xiangliang P, Lanhai L, Zhongqin L (2012) Ponder on the issues of water resources in the arid region of northwest China. *Arid Land Geogr* 35(1):1–9
- Yi Liu (2019) Why Northwest China is "warming and humidifying". *People's Daily*, 15
- Zaremehrjardy M, Razavi S, Faramarzi M (2021) Assessment of the cascade of uncertainty in future snow depth projections across watersheds of mountainous, foothill, and plain areas in northern latitudes. *J Hydrol* 598:125735
- Zhang Y, Long A, Lv T, Deng X, Wang Y, Pang N, Lai X, Gu X (2023) Trends, cycles, and spatial distribution of the precipitation, potential evapotranspiration and aridity index in Xinjiang, China. *Water* 15(1):62
- Zhang Z (2018) Modeling hydrological processes in main runoff generating area of Manasi river basin, Xinjiang. PhD thesis, Shihezi University, Shihezi City, China

Publisher's Note Springer Nature remains neutral with regard to jurisdictional claims in published maps and institutional affiliations.